CrossMark

The First Multichroic Polarimeter Array on the Atacama Cosmology Telescope: Characterization and Performance

S. P. Ho[1] · **C. G. Pappas**[1] · **J. Austermann**[2] · **J. A. Beall**[2] · **D. Becker**[2] ·
S. K. Choi[1] · **R. Datta**[3] · **S. M. Duff**[2] · **P. A. Gallardo**[4] · **E. Grace**[1] ·
M. Hasselfield[1] · **S. W. Henderson**[4] · **G. C. Hilton**[2] · **J. Hubmayr**[2] ·
B. J. Koopman[4] · **J. V. Lanen**[2] · **D. Li**[2] · **J. McMahon**[3] · **F. Nati**[5] ·
M. D. Niemack[4] · **P. Niraula**[1] · **M. Salatino**[1] · **A. Schillaci**[1] · **B. L. Schmitt**[5] ·
S. M. Simon[1] · **S. T. Staggs**[1] · **J. R. Stevens**[4] · **J. T. Ward**[5] · **E. J. Wollack**[6] ·
E. M. Vavagiakis[4]

Abstract The Atacama Cosmology Telescope Polarimeter (ACTPol) is a polarization sensitive receiver for the 6-m Atacama Cosmology Telescope (ACT) and measures the small angular scale polarization anisotropies in the cosmic microwave background (CMB). The full focal plane is composed of three detector arrays, containing over 3000 transition edge sensors (TES detectors) in total. The first two detector arrays, observing at 146 GHz, were deployed in 2013 and 2014, respectively. The third and final array is composed of multichroic pixels sensitive to both 90 and 146 GHz and saw first light in February 2015. Fabricated at NIST, this dichroic array consists of 255 pixels, with a total of 1020 polarization sensitive bolometers and is coupled to the telescope with a monolithic array of broad-band silicon feedhorns. The detectors are read out using time-division SQUID multiplexing and cooled by a dilution refrigerator at 110 mK. We present an overview of the assembly and characterization of this multichroic array

---

✉ S. P. Ho
   spho@princeton.edu

1   Department of Physics, Princeton University, Princeton, NJ 08540, USA

2   NIST Quantum Devices Group, 325 Broadway, Mailcode 817.03, Boulder, CO 80305, USA

3   Department of Physics, University of Michigan, Ann Arbor 48103, USA

4   Department of Physics, Cornell University, Ithaca, NY 14853, USA

5   Department of Physics and Astronomy, University of Pennsylvania, 209 South 33rd Street, Philadelphia, PA 19104, USA

6   Goddard Space Flight Center, National Aeronautics and Space Administration, Greenbelt, MD 20771, USA

in the lab, and the initial detector performance in Chile. The detector array has a TES detector electrical yield of 85 %, a total array sensitivity of less than 10 $\mu K \sqrt{s}$, and detector time constants and saturation powers suitable for ACT CMB observations.

1 Introduction

From observations of the CMB, experiments now focus on the polarization of the CMB, acting as an additional probe of cosmology containing information complementary to that encoded in the temperature anisotropies. Detection of the faintest polarized signals requires instruments with high sensitivity and multiple frequency bands for foreground removal [1]. Multichroic polarimeters provide a method to detect galactic foregrounds within a single focal plane sensitive to multiple frequency bands.

In this paper, we present the design, assembly, and performance of a multichroic detector package which is deployed as the third array, Polarimeter Array 3 (PA3) in the ACTPol receiver. It was deployed in January 2015, and employs 1020 detectors sensitive to 90 and 146 GHz simultaneously. A dilution refrigerator is used as the cooling system for the entire receiver, and maintains a continuous operating bath temperature of $\lesssim$110 mK.

2 Multichroic Array

2.1 Array Design

The PA3 (Fig. 1) uses the same array format as the first two deployed ACTPol arrays. It has three hexagonal (hex) and three semi-hexagonal (semihex) detector array stacks with 61 pixels per hex wafer and 24 pixels per semihex wafer composing a total of 255 pixels. The array consists of ortho-mode transducer (OMT)-coupled transition-edge sensor (TES) bolometers. The radiation goes onto the OMT, which is at the center of the TES detector pixel, then the two polarization signals are separated by

Fig. 1 The fully assembled PA3 is shown from the non-sky side, with six sub-wafers sitting in the center and with the PCBs sitting around the edge and perpendicular to the detector wafers (Color figure online)
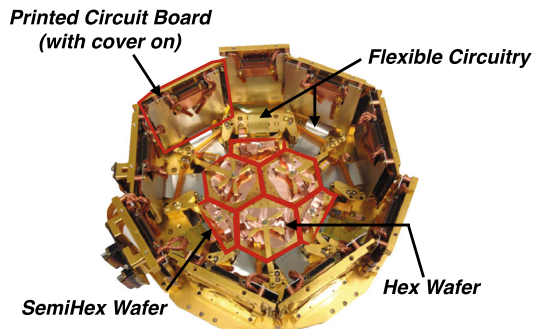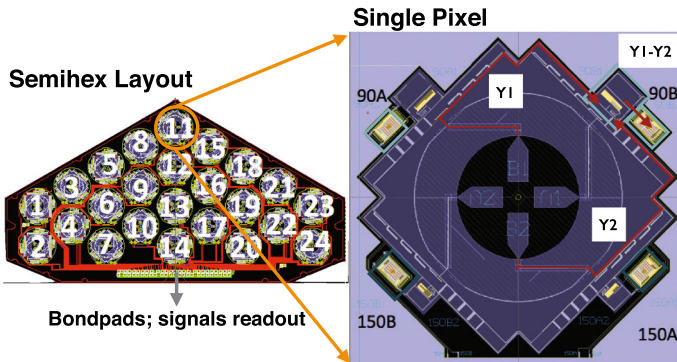
Fig. 2 *Left* the layout of two semihex wafers. *On the top* wafer, the numbers list the 24 pixels in one semihex wafer. *Right* the layout of pixel, the electrical signal path is shown in *red lines*, details can be read in [2] (Color figure online)

opposing pairs of the antenna and carried through niobium microstrip lines, and stub band-pass filters to their respective TES islands. The island has four silicon nitride legs weakly thermal-linking to the bath, held at a base temperature, T_{bath}. The TES devices are made of molybdenum–copper (MoCu), with a critical temperature T_c of ~146 mK [2]. The resistance versus temperature relationship of the superconducting TES detectors enables sensitive measurements of the incident power. The pixel design is shown in Fig. 2 and described in detail in Datta et al. [2]. Each multichroic pixel has four bolometers, two for each polarization observing in each optical frequency band, matching the number of detectors to the other two arrays.

The beam pattern of the full array is defined by a broad-band ring-loaded corrugated feed horn. Five ring-loaded sections allow for a broad-band impedance matching transition between the round input waveguide and corrugated output waveguide.

Measurements of these horn-coupled single pixels show detector optical efficiencies of 70 and 76 % respectively, for the 90 and 146 GHz bands, not including the optics inside the receiver.

During CMB observations, the TES detectors are voltage-biased. As the telescope scans across the sky, changes in the TES detector current are measured to determine changes in the observed optical signal. To read out the TES detector currents, we use a 32 column by 32 row superconducting quantum interference device (SQUID) time-division multiplexing (TDM) scheme with three stages of SQUID amplification [3].

2.2 Array Assembly

The first-stage readout printed circuit boards (PCBs) are mounted perpendicular to the focal plane to reserve the focal plane area for TES detector pixels as shown in Fig. 1. Superconducting aluminum flexible circuits (flex) connect the detector wafers to the

first-stage readout. The PCBs are at the same bath temperature as the detector wafers are. The PA3 has a 85 % yield on the telescope; the improvement comes from the robust electrical connections from the detector wafer to the readout chips. Electrical connections between the flex, readout chips, detector wafer, and PCB are all aluminum wire bonds made with an automatic wedge wire bonder. Due to advancements in assembly techniques, the increase in yield from the previous two arrays to PA3 was mainly due to the bondability of the flex used.

For PA3 hex wafers(which counts for two-third of the array), two-layer flex with 200 µm pitch produced by Tech-Etch [4] were used, same as the previous two arrays in the receiver, but the stiffeners are changed from copper to silicon, providing a hard substrate surface for bonding. The silicon stiffeners were mounted with epoxy using a flip-chip bonder to ensure proper alignment and prevent air bubbles from forming between the flex and stiffener. This method improved the average yield of detectors unaffected by multiplexing-line failures from 84 to 92 %. In the rest one-third of the array, a new type of Flex fabricated at Princeton [5] was fielded for CMB observations for the first time on the sky. The flex is single-layer with a 110-µm trace pitch. As described in Pappas et al. [5], the flex used to assemble the semihex detectors in this array features bond pads that sit on a hard silicon substrate, so wire bonding to these flex is as robust as to silicon chips. The average yield of the semihex detectors unaffected by second-stage SQUID column failures was 92 %, with the failures due mainly to some imperfections in the flex that were observable in room temperature probing.

With these amendments in assembly, the PA3 yield was successfully improved by 25 and 15 % for the first and second arrays, respectively.

3 Multichroic Array Performance

To optimize the detector performance on the sky, the detector thermal noise, detector time response, and operating loading condition. The detector thermal conductance G contributes to the thermal noise ; the loading conditions, like the precipitation water vapor (PWV) in the day, can affect biasing the detectors in proper range, thus setting the optimal detector saturation power, P_{sat}, during fabrication is critical; the detector response, obtained by calculating time constant (τ) of the detectors, is related to the detector sensitivity. If G and P_{sat} are too low, the detectors cannot be biased in the presence of optical loading P_γ; if G and T_c are too high, thermal noise will dominate over the sky noise resulting the signal from the sky invisible. P_{sat} also affects the characteristic time constant by which the detector responds to a change in signal (see Sect. 3.2). Taking these three constraints into account: minimizing the thermal noise, ensuring the detectors would not saturate under normal loading conditions (where the PWV below 1 mm), and matching the time constant target, we chose a P_{sat} target of 10–14 pW for PA3. The time constant, inversely proportional to the detector sensitivity, implies that the faster the detectors are, the more sensitive they are to the signals, which holds when the readout sampling rate allows.

Detector sensitivity is quoted using noise equivalence power (NEP), which is the minimum power to put on a detector to get the signal-to-noise ratio of 1. The median

G and T_c values imply a dark NEP of 2.0×10^{-17} W/$\sqrt{\text{Hz}}$. With $\sim$2 pW of load on the detectors (using a cover to block most of the sky signal), contributing $\sim$2.6 $\times$ 10^{-17} W/$\sqrt{\text{Hz}}$ to the NEP, we measure a median NEP of 3.4×10^{-17} W/$\sqrt{\text{Hz}}$, in good agreement with the anticipated quadrature sum of 3.3×10^{-17} W/$\sqrt{\text{Hz}}$.

All these parameters above would contribute later to the array sensitivity, which is measured by the detector response to an optical pulse in the form of planet observations versus the detector noise spectrum. The optical efficiency and spectral response of the detectors is discussed in Datta et al. [6]. Under normal observing conditions, when the PWV is less than 1 mm, the total array sensitivity (combining the 90 and 146 GHz bands) is less than 10 μK/$\sqrt{\text{Hz}}$.

3.1 Saturation Power

We define the P_{sat}, as the thermal power on the TES detector island necessary to drive the TES detector to T_c, which we define as the bias power at 90 % of the normal resistance (R_n), $0.9R_n$. The logarithmic current sensitivity, β is low when high on the superconducting transition, the TES detector temperature at $0.9R_n$ is approximately constant, independent of TES detector bias current (see, e.g., [7]). The P_{sat} of the detector is related to T_c and the thermal conductance (G) between the TES detector island and the bath via a power law dependence [8],

$$P_{\text{sat}} = \kappa(T_c^n - T_{\text{bath}}^n) = P_{\text{bias}}(0.9R_n) + P_\gamma, \tag{1}$$

$$G = dP_{\text{sat}}/dT|_{T_c} = n\kappa T_c^{n-1}, \tag{2}$$

where n and κ are determined by the geometry and material properties of the TES detector legs.

As discussed above, a detector's P_{sat} at the operating bath temperature depends on the TES detector T_c and the thermal conductivity between the TES detector island and the bath, parametrized by κ and n. We measure these values by taking IV curves (recording the TES detector current as we vary the voltage across it) under dark conditions at a series of bath temperatures and measure P_{bias} at $0.9R_n$ for each. We then fit Eq. 2 with $P_\gamma = 0$ to the data to solve for κ, n, and T_c. These measurements were performed in a dark cryostat in the lab before deployment and in the telescope with the window covered.

Observations are done at a base temperature (110 mK), but precise temperature control for temperatures above this has not yet been well optimized. We use the lab data for a subset of detectors (from the hex wafer called FH4) to calibrate the telescope data as follows: Consider a reference detector (1) for which we have precise lab values of κ_1 and T_{c1}. We plot its $P_{\text{bias}}(0.9R_n)$ from telescope data versus those from a detector poorly measured in the lab (2). Assuming all detector wafers are at the same T_{bath}, we have

$$mP_{\text{bias}}(.9R_n)_1 + b = P_{\text{bias}}(.9R_n)_2, \text{ with } m = \kappa_2/\kappa_1, b = \kappa_2(T_{c2}^n - T_{c1}^n). \tag{3}$$

We can then convert κ_2 and T_{c2} to absolute values. In practice, we use laboratory measurements of κ and T_c of the FH4 detectors during an individual detector wafer cool down, when we knew T_{bath} very well, to convert these numbers to absolute κ and T_c values. Because a slightly different estimate of κ and T_c is found from comparing to the different detectors in FH4, the median across these detectors is used.

Spatial plots for the array parameters are shown in Fig. 3. There are some variations between detectors; nonetheless, it is more important that the group of detectors on one bias line has uniform enough P_{sat} values so that they can all be biased well at one bias voltage. Fig. 3g shows that when we target the biasing at 50 % R_n, the PA3 P_{sat}s are uniform enough for each set of detectors to share a voltage bias line, i.e., 95 % of the detectors are biased within 30–70 % R_n.

3.2 Time Constants

The detector effective time constant τ_{eff} determines the extent to which the detector response at high frequencies is filtered. The intrinsic thermal time constant is given as
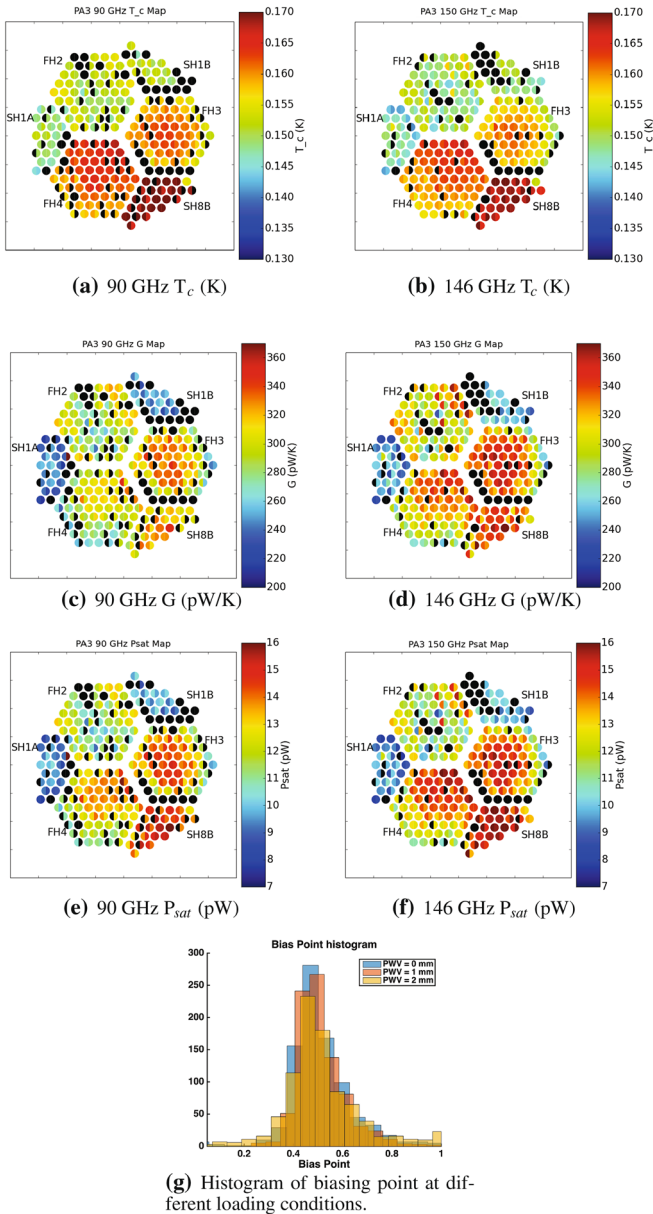
$$\tau = \frac{C}{G},\tag{4}$$

which can be tuned by varying the heat capacity C of the TES detector island through the addition of PdAu [9]. Following Irwin & Hilton [8,10] and Niemack [11], we can relate $f_{3dB} \equiv (2\pi\tau_{eff})^{-1}$, or frequency with 50 % of the response, to the bias power P_{bias} applied to the TES detector:

$$f_{3dB} = \frac{1}{2\pi}\left(\tau^{-1} + \frac{\alpha}{(1+\beta)}\frac{1}{T_cC}P_{bias}\right).\tag{5}$$

The transition shape is described by $\alpha \equiv \frac{T}{R}\frac{dR}{dT}$, and $\beta \equiv \frac{I}{R}\frac{dR}{dI}$ [8]. This equation shows a dependence of the time constants on the bias conditions of the TES detectors [11].

The detector time constants in ACTPol are calibrated by planet observations and bias steps to calibrate the detector time constants(See Fig. 4). For planet observations, a finite time constant causes a shift in the apparent source peak position when scanning a point source from two opposite scan positions. For bias step, the time constant is measured by fitting the edge of the TES detector current response to a small voltage square wave on its voltage bias line [12]. The planet observations are a direct method to obtain time response, however, we can do bias step measurements much more frequently than planet scans. Thus we track the variability of the f_{3dB}s at different loading conditions with bias steps calibrated per detector from the Uranus measurements.[1] Figure 5 shows histogram of the values from bias step method. Because the sampling rate is 400 Hz, measurements of $f_{3dB} > 200$ Hz are poorly constrained. Fortunately, the filtering effect caused by such fast time constants is negligible at the

---

[1] The analysis to estimate time constants from planet scans includes deconvolution of the 200 Hz digital anti-aliasing filter used for the science data-taking mode.

(a) 90 GHz T$_c$ (K)

(b) 146 GHz T$_c$ (K)

(c) 90 GHz G (pW/K)

(d) 146 GHz G (pW/K)

(e) 90 GHz P$_{sat}$ (pW)

(f) 146 GHz P$_{sat}$ (pW)

(g) Histogram of biasing point at different loading conditions.

Fig. 3 Detector properties, T_c, P_{sat}, and G, as a function of array position. In the array plots, three hexagonal wafers and three semi-hexagonal wafers compose of a full 6-inch hexagonal array. Each circle represents one detector, with two values shown per pixel for two polarizations. Black indicates missing data or non-functioning detectors. The array is connected to the bath through a thermal heat sink from the lower right of the figure (wafer SH8B). **a** and **b** Critical temperature, 90 GHz and 146 GHz medians are 158 $\pm$ 8 and 155 $\pm$ 8, respectively. **c** and **d** Thermal conductivity, using n = 3.4, 90 and 146 GHz medians are 285 $\pm$ 30 and 300 $\pm$ 40, respectively. **e** and **f** P_{sat} at $T_{bath} \sim$ 110 mK, 90 GHz and 146 GHz medians are 9 $\pm$ 2 and 10 $\pm$ 2, respectively. **g** At different loading conditions, we can bias 95 % of the detectors within the target percent R_n, 50 % R_ns (Color figure online)
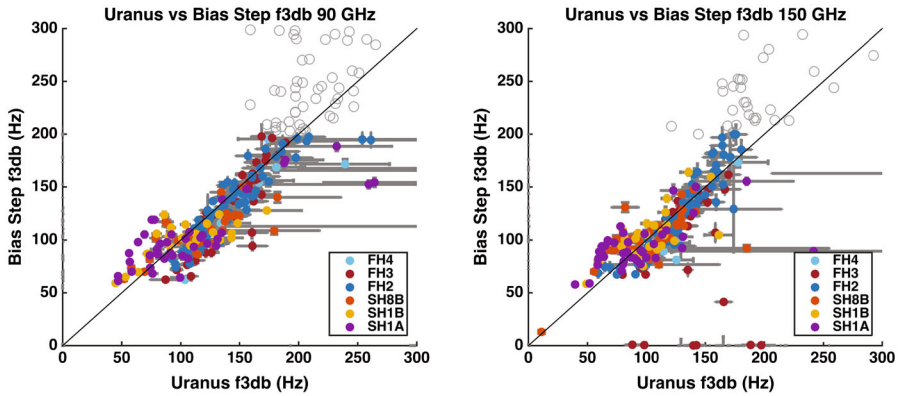
Fig. 4 The measured f_{3dB} values from bias step measurements and derived from scans of uranus. Each data point is the average of the time stream data collection from 32 files of separate uranus observations. *Error bars* are calculated from the variance of these multiple observations through a range of loading conditions. The *left* shows the f_{3dBs} from 90 GHz detectors and the *right* is the f_{3dBs} from 146 GHz ones, with *colors* indicating different wafers on the arrays. These plots show the stability of the f_{3dBs} of individual wafer getting from the bias step measurements, which has smaller *error bars* over different loading conditions. The *gray circles* indicate detectors whose determination of f_{3dBs} is poorly constrained due to the 400 Hz sampling (Color figure online)

(a) PA3 90 GHz   **(b)** PA3 146 GHz
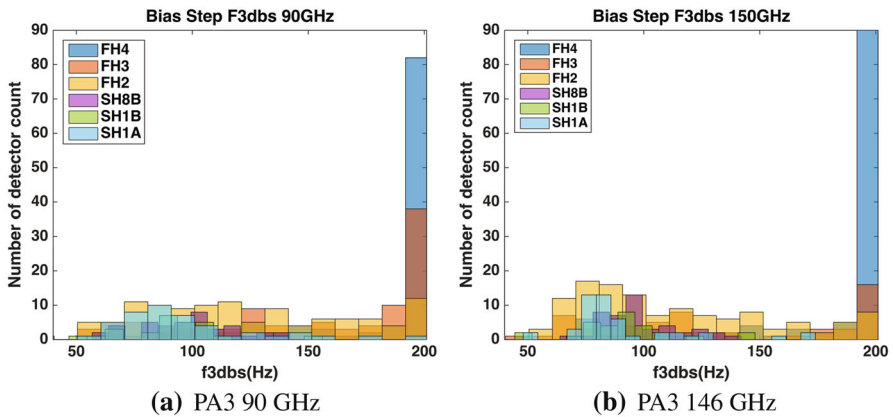
Fig. 5 Histograms of the time constants of the PA3 90 GHz (*left*) and 146 GHz detectors (*right*), illustrating that nearly all detector responses are faster than 50 Hz as desired. All f_{3dBs} above 200 Hz are binning to the last bin since the readout rate is too slow to see the exponential response when it is faster than 200 Hz so the measurement is poorly constrained (Color figure online)

frequencies containing the CMB signal. In the histograms, most f_{3dBs} are above 50 Hz, which give a rough guideline for future data cuts.

4 Conclusion

The first multichroic detector array is deployed and observed on ACT. The detector array was robustly assembled with a TES detector yield of 85 %. The detectors are

highly sensitive, with an overall array sensitivity less than $10\,\mu\mathrm{K}\sqrt{\mathrm{s}}$. The P_{sat}s of the detectors are high enough that they do not saturate under normal observing conditions. There is also good P_{sat} uniformity within each bias line so that 95 % of the detectors can be biased within 30–70 % R_n. The detector time constants are well suited for ACT observations, with most detector f_{3dBs} above 50 Hz.

References

1. Planck Collaboration et al., Planck intermediate results. XXX. The angular power spectrum of polarized dust emission at intermediate and high Galactic latitudes. arXiv:1409.5738v2. doi:10.1051/0004-6361/201425034
2. R. Datta et al., J. Low Temp. Phys. **176**(5), 670–676 (2014). doi:10.1007/s10909-014-1134-4
3. J.A. Chervenak et al., Appl. Phys. Lett. **74**, 26 (1999)
4. Tech-Etch company, http://www.tech-etch.com/
5. C.G. Pappas, IEEE Trans. Appl. Supercond. **25**, 1 (2015). doi:10.1109/TASC.2014.2379092
6. R. Datta et al., J. Low Temp. Phys. doi:10.1007/s10909-016-1553-5
7. D.A. Bennett et al., J. Low Temp. Phys. **167**(3–4), 102–107 (2012). doi:10.1007/s10909-011-0431-4
8. K.D. Irwin, G.C. Hilton, *Cryogenic Particle Detection* (Springer, Berlin, 1994)
9. E.M. George et al., J. Low Temp. Phys. **176**, 383–391 (2013). doi:10.1007/s10909-013-0994-3
10. K. Irwin, G. Hilton, *Transition-Edge Sensors. Cryogenic Particle Detection* (Springer, Berlin, 2005)
11. M.D. Niemack, Ph.D. Thesis, Princeton University, 2008
12. E.A. Grace et al., J. Low Temp. Phys. **176**, 705 (2014). doi:10.1007/s10909-014-1125-5